This article has been accepted for publication in a future issue of this journal, but has not been fully edited. Content may change prior to final publication. Citation information: DOI 10.1109/TIM.2020.2994433, IEEE Transactions on Instrumentation and Measurement



# Wideband Near-Zone Radiative System for Exploring the Existence of Electromagnetic Emission from Biological Samples

S. Mohammad Amjadi, *Member, IEEE*, Menglou Rao, *Student Member, IEEE*, and Kamal Sarabandi, *Fellow, IEEE*

***Abstract*—This work reports on a wideband near-zone radiative system operating from 1 to 50 GHz for examining the possibility of electromagnetic emission from a community of bacteria in a petri dish or any other distributed sources confined in a small focusing area. The system includes a dual-polarized signal collector, a Dicke switch, broadband low-noise amplifiers (LNAs) and a precision spectrum analyzer. The signal collector is composed of a quadruple-ridged horn-type structure of dimensions $\boldsymbol{\lambda_L \times \lambda_L \times 1.6\,\lambda_L}$ (where $\boldsymbol{\lambda_L}$ is the wavelength at the lowest frequency) having two orthogonal probes. The provision of a dielectric cone along the horn central axis allows for collimating the waves in the focusing area over the entire bandwidth. Therefore, the signal collector acts as a field concentrator to provide a uniform field distribution across the focusing area (source location). The entire structure is designed to be EM-shielded and free from resonance. It can effectively exclude outside interference while maintaining a uniform collection of the electromagnetic spectrum.**

***Index Terms*— Distributed sources; dual-polarized sensor; electromagnetic signaling; wideband radiative sensor.**

## I. Introduction

Although there are many hypotheses about purposeful electromagnetic wave signaling between biological cells in the literature [1]-[3], no experiments have proved the existence of such signals in the GHz frequency range so far. The spectrum and the power level of such signals, if they do exist, are still unknown. Recent theoretical models suggest that radiation may happen somewhere between 1 to 50 GHz, depending on the physical parameters of cells, and the power level is expected to be on the same order as that of thermal noise. In order to explore the existence of radiation from biological samples, an ultra-wideband system with very high sensitivity is needed to perform the necessary measurements.

Radiative probes have several advantages over non-radiative capacitive probes such as coaxial probes which makes them more reliable for sensing the collected electromagnetic wave emanated from distributed sources. Non-radiative high-impedance probes capture the electromagnetic waves through their very near-field region which is limited to the very small contact area around the tip of the probe [4]. In addition, the presence of the probe may significantly affect the environment and the field distribution of the sources producing the field. Another drawback of capacitive probes is their small collection area. Moreover, the probe should be in very close proximity of the source and is sensitive to positioning. Finally, half of the power is missed due to polarization mismatch. Different radiative probes such as TEM cells have been reported to measure radiation from electromagnetic sources or generate uniform electric field over a wide bandwidth [5-11]. The first TEM cell was introduced by Crawford in 1974 [5]. Since then different shielded or unshielded TEM cells have been reported for different purposes including characterization of radiation from printed circuit boards [6], estimation of electromagnetic emission from electrically large equipment [7],[8], and pulse-exposure studies of biological specimen [9]. The bandwidth of TEM cells are limited by cutoff frequency of the higher order modes. In [10], by suppressing higher order modes, a TEM cell design with 85% fractional bandwidth operating from 1 GHz to 2.5 GHz is reported. However, for certain applications where the spectrum of the emitted signal is not known, a system capable of detecting signals over multiple octave bandwidth is required. Moreover, TEM cells only capture a single polarization which makes them deficient for detection of EM signals emanated from a collection of randomly oriented sources. To address these problems, an EM-shielded and resonance-free structure is presented which allows for capturing electromagnetic emission from a collection of distributed radiators confined in an area of $0.15\,\lambda_L \times 0.15\,\lambda_L$ placed inside the structure. This large sample size help increase the received Signal-to-Noise Ratio (SNR). The signal collector is designed to capture two orthogonal polarizations from 1 to 50 GHz. Signals from each port are amplified by two cascaded low-noise amplifiers (LNA) and are recorded individually by a spectrum analyzer. A Dicke switch is used in each path to calibrate the measured data to a constant noise source. One of the

The authors are with the Radiation Laboratory, Electrical Engineering and Computer Science Department, University of Michigan, Ann Arbor, MI 48109-2122, USA (e-mail: smamjadi@umich.edu; menglrao@umich.edu; saraband@umich.edu).

This work was supported by the U.S. Defense Advanced Research Projects Agency (DARPA).

This article has been accepted for publication in a future issue of this journal, but has not been fully edited. Content may change prior to final publication. Citation information: DOI 10.1109/TIM.2020.2994433, IEEE Transactions on Instrumentation and Measurement


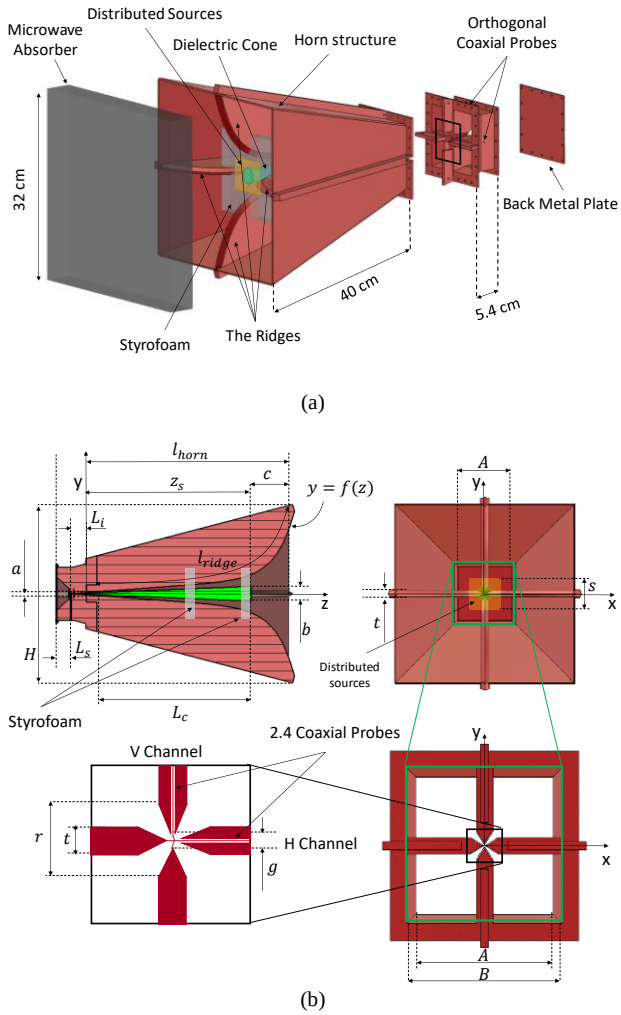


Fig. 1: The wideband dual-polarized signal collector.

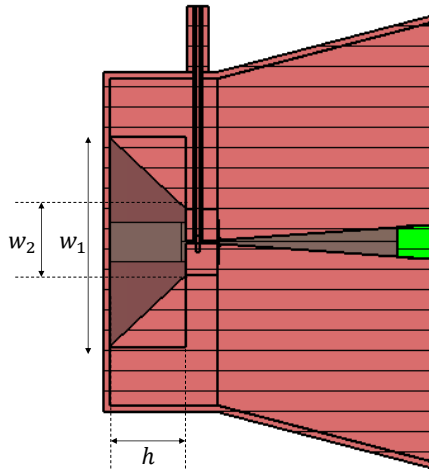


Fig. 2: The quadruple-ridged cavity of the feed section.

TABLE I
OPTIMIZED VALUES OF THE STRUCTURE SHOWN IN FIG. 1

| Parameter | Value (mm) | Parameter | Value (mm) |
|---|---|---|---|
| $H$ | 320 | $g$ | 1.1 |
| $l_{horn}$ | 420 | $A$ | 100 |
| $c$ | 75 | $B$ | 113 |
| $L_c$ | 280 | $r$ | 20 |
| $a$ | 9.5 | $s$ | 50 |
| $b$ | 29 | $t$ | 12 |
| $L_i$ | 35 | $L_s$ | 27 |
| $z_s$ | 404 | $w_1$ | 64 |
| $h$ | 23.5 | $w_2$ | 20 |
| $l_{ridge}$ | 510 | | |

applications of this system is for investigation on the existence of electromagnetic signaling between biological cells [12]. These biofilms are grown in a petri dish with an area of $4.5\ cm \times 4.5\ cm$. Thereby, the EM-shielded structure should be designed to not only accommodate the petri dish but also to generate a concentrated electric field over the region where the petri dish is placed. In Section II, the structure of the signal collector is presented. The wideband radiometer system which is built based on the proposed near-zone radiative signal collector is described in Section III. To validate the sensitivity of the system, exemplary measurements on thermal radiation from water samples with slightly different temperature are conducted and presented in Section IV. Experiments with biological samples are currently in progress and the results will be reported in the future.

## II. WIDEBAND RADIATIVE SIGNAL COLLECTOR

The wideband dual-polarized signal collector is shown in Fig.1. A quadruple-ridged horn structure backed by an absorber is used for EM shielding. The quadruple-ridged waveguide structure is chosen to increase the bandwidth towards lower frequencies through reducing the cutoff frequency of the dominant mode [13]. Terminating the aperture of the horn by the absorber has the advantages of isolating the sample from possible external interferences and of creating a resonance-free environment within the band of operation. Since the absorber acts as a semi-infinite half space, it ensures the surrounding lab environment does not influence the measurement without disturbing the input impedance and field distribution of the signal collector. The downside of using the absorber is that for isotropic distributed source, half of the power is dissipated in the absorber. The structure is probed by two high frequency coaxial lines. The back of the feed section is terminated by an optimized ridged cavity with a linear tapered ridge profile for

This article has been accepted for publication in a future issue of this journal, but has not been fully edited. Content may change prior to final publication. Citation information: DOI 10.1109/TIM.2020.2994433, IEEE Transactions on Instrumentation and Measurement


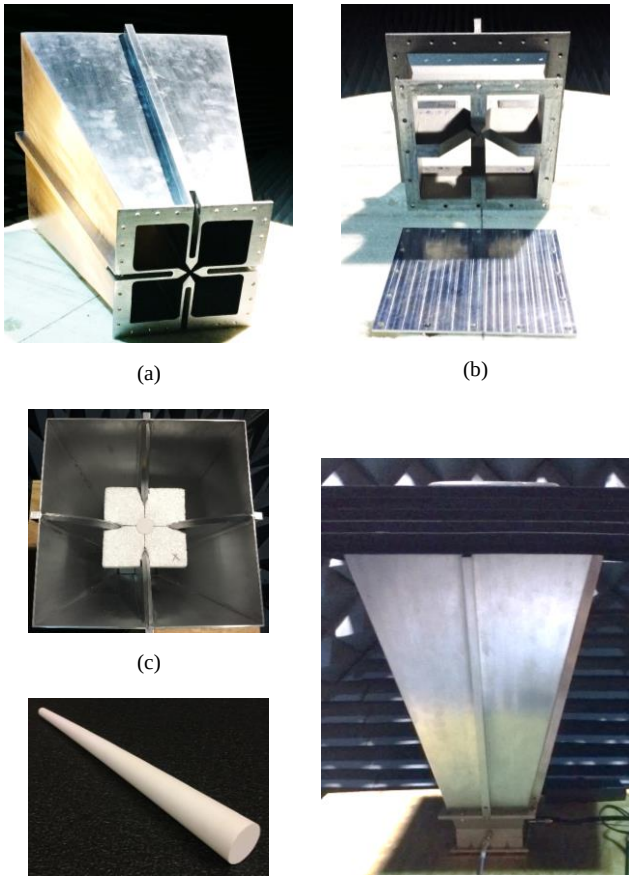


Fig. 3 The fabricated dual-polarized signal collector. (a) the horn structure, (b) the feed section, (c) the ridges inside the horn, (d) the dielectric cone, and (e) the assembled structure.

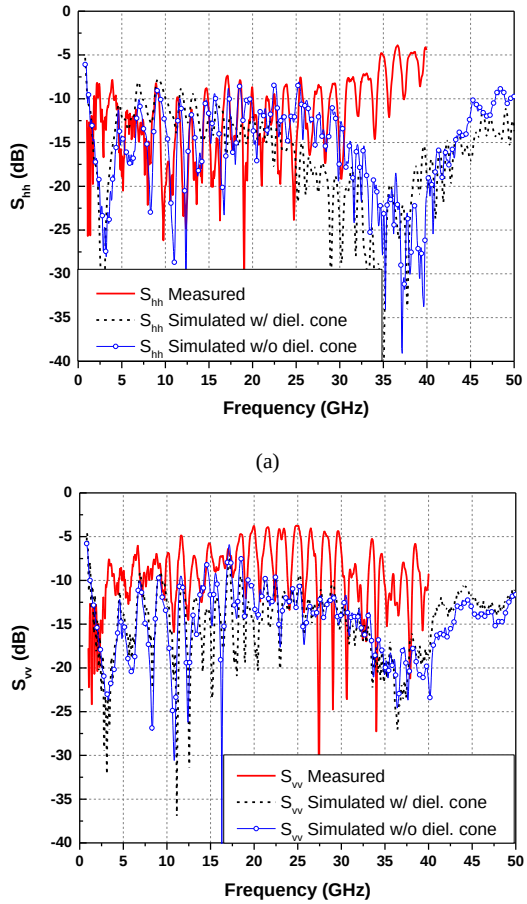


Fig. 4 The simulated and measured S-parameters of (a) hh-polarization and (b) vv-polarization of the collector.

impedance matching as shown in Fig.2. The size and tapering of the ridges and the horn angle are optimized to achieve the maximum bandwidth and the desired field distribution. A combination of linear and exponential function is used to improve the impedance match bandwidth [14]. With reference to Fig.1, the profile of the ridge curvature is given by:

$$y = (1-m)\left(a_i + (a_0 - a_i)\frac{z - L_i}{L}\right) + A\left(c_1 e^{R(z-L_i)} + c_2\right) \tag{1}$$

where

$$c_1 = \frac{a_0 - a_i}{e^{RL} - 1} \tag{2}$$

$$c_2 = \frac{a_i e^{LR} - a_0}{e^{RL} - 1} \tag{3}$$

and $m = 0.8, a_i = r/2$ , $a_0 = H/2$ , $L = l_{horn} - L_i$, and $R = 0.03$. A dielectric cone is inserted in the middle to slow down the phase front of the wave in the center of the structure so that a uniform phase distribution over a very wide bandwidth can be

This article has been accepted for publication in a future issue of this journal, but has not been fully edited. Content may change prior to final publication. Citation information: DOI 10.1109/TIM.2020.2994433, IEEE Transactions on Instrumentation and Measurement


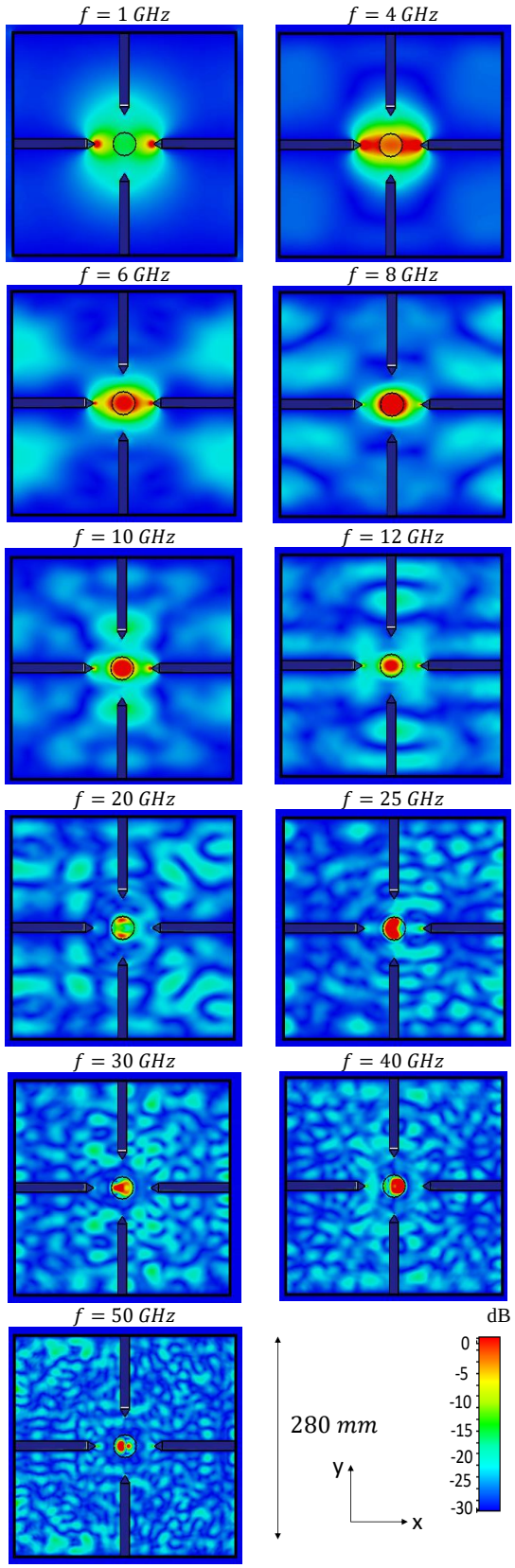


Fig. 5 (a) Simulated field distribution with the dielectric cone at $z = z_s$ (the base of the dielectric cone) when the x-oriented probe is excited.

established at the base of the cone. The dielectric also assists with maintaining the field to be concentrated at the center all along the horn axis towards its opening where the sample is located. To correct for the phase difference between the waves traveling along the ridge and through the center of the horn, the dielectric constant of the cone can approximately be calculated from

$$\varepsilon_r \approx \left(\frac{l_{ridge}}{l_{horn}}\right)^2 \tag{4}$$

The optimized values of the parameters are listed in Table. I. The horn structure is made from two parts. The top section (the aperture side) is fabricated by accurate CNC Aluminum machining and welding. The lower section (the feed side) is 3D printed out of AlSiMg. These sections are shown in Fig. 3(a) and 3(b) respectively. High frequency $2.4\ mm$ coaxial connectors are used for probing the signal from the collector. To assemble the coaxial probes, two holes are created in the walls of the feed section which extend through the ridges as depicted in Fig.2. A brass bolt with an axial through-hole is used to connect the cable to the feed section. The coaxial cable is passed through the hole in the bolt and the outer conductor of the cable is soldered to the bolt. The bolt is then screwed to the waveguide body and the inner conductor of the cable is inserted into a blind hole on the ridge on the opposite side and is fixed in place using silver epoxy. The vertical and horizontal probes are spaced by $1.5\ mm$ along the axis of the structure. The dielectric cone is fabricated from ECCOSTOCK® LoK material with $\varepsilon_r = 1.7$ by CNC machining. Two Styrofoam holders are used to keep the dielectric cone in place. The biological sample is sized to be able to sit on the upper Styrofoam at the base of the cone. The fabricated parts and the assembled structure are shown in Fig.3. The simulated S-parameters with and without the dielectric cone are illustrated in Fig.4 along with the measurement results. The presence of the dielectric cone does not significantly affect the input impedance of the signal collector. The measured reflection coefficients are less than $-6.5$ dB over the entire band, which translates to more than 77.6% transmission of the energy from the sample to the system. The simulated field distribution at $z = z_s$ (the base of the dielectric cone) with and without the dielectric cone at different frequencies are depicted in Fig.5 (a) and (b). Without the dielectric cone, the electric field diverges at the aperture,

This article has been accepted for publication in a future issue of this journal, but has not been fully edited. Content may change prior to final publication. Citation information: DOI 10.1109/TIM.2020.2994433, IEEE Transactions on Instrumentation and Measurement


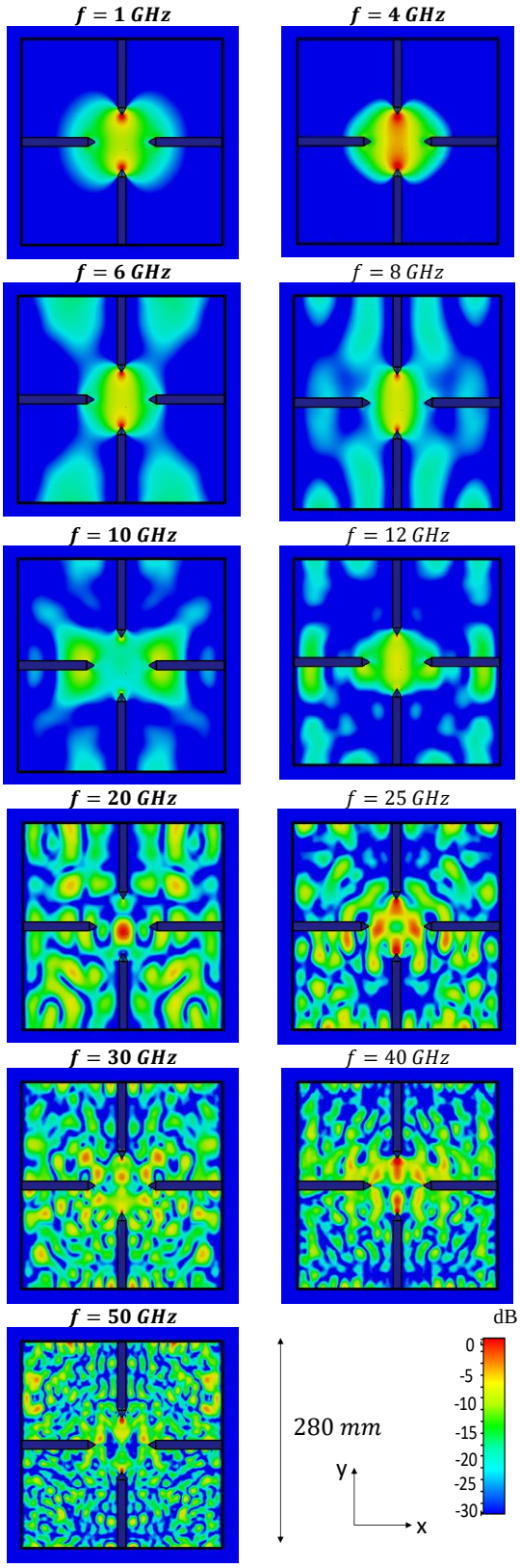


Fig. 5(b) Simulated field distribution without the dielectric cone at $z = z_s$ when the x-oriented probe is excited.

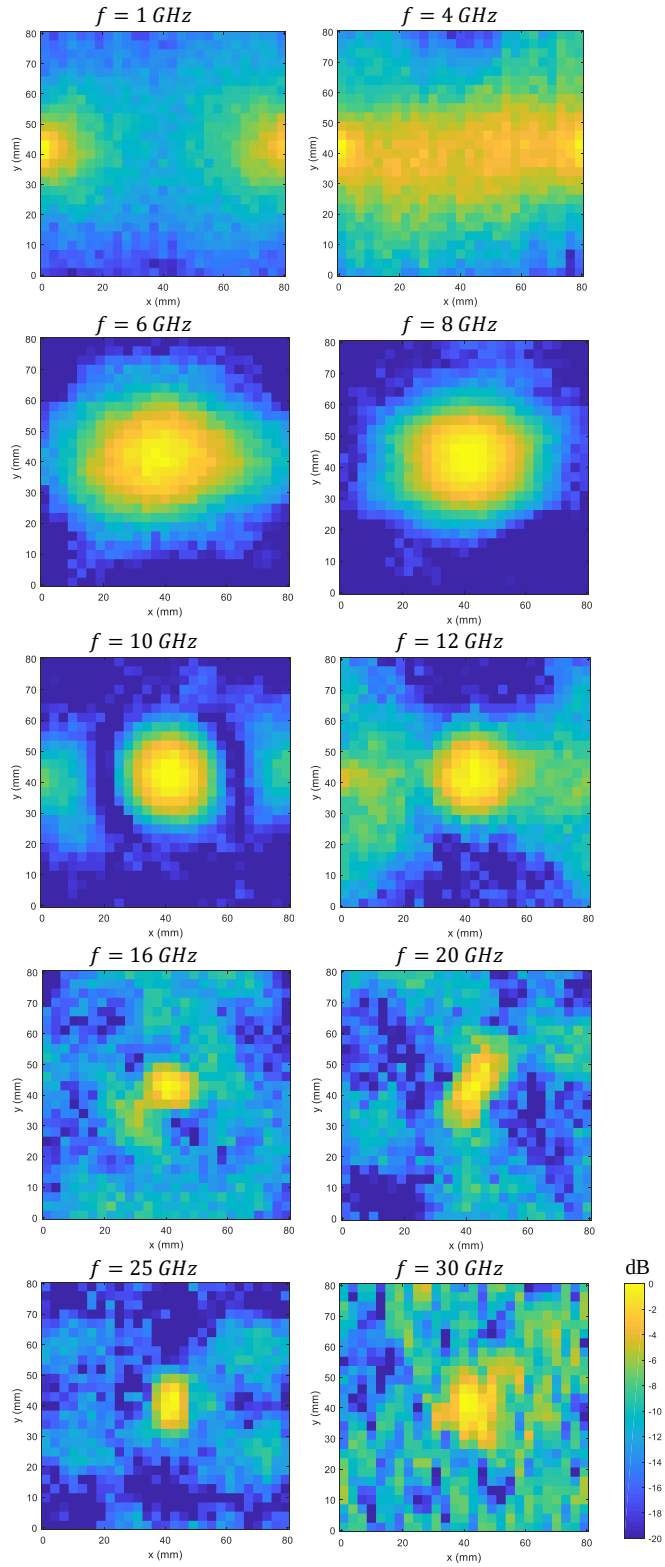


Fig. 6: The normalized measured field distribution at $z = z_s$ (the base of the dielectric cone) using NeoScan measurement system.

This article has been accepted for publication in a future issue of this journal, but has not been fully edited. Content may change prior to final publication. Citation information: DOI 10.1109/TIM.2020.2994433, IEEE Transactions on Instrumentation and Measurement


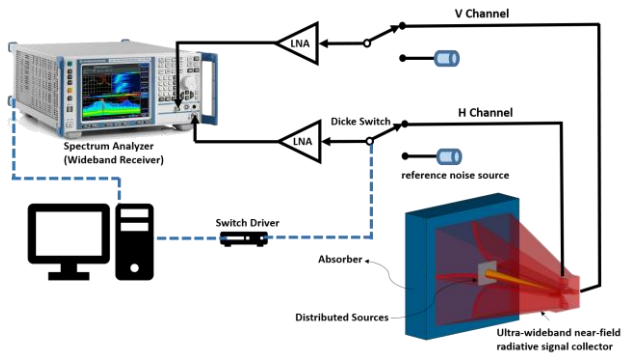


Fig. 7: The wideband radiometer setup

whereas with the dielectric cone, the electric field is collimated at the base of the cone, where the radiating sample sits, at all frequencies. Below 4 GHz, a spike in the electric field is observed in the E-plane around the tip of the ridge. The size of the focusing area varies from $5\,cm \times 5\,cm$ at low frequencies to $2\,cm \times 2\,cm$ at high frequencies. The measured field distribution at $z = z_s$ over an area of $8\,cm \times 8\,cm$ using NeoScan field measurement system [15] is plotted in Fig.6. The NeoScan probe is an electro-optic field probe with a crystal optic tip attached to an optical fiber. The probe tip is of dimensions $1mm \times 1mm \times 1mm$. The measurement is performed over an area of $80\,mm \times 80mm$ in xy-plane with a resolution of $3\,mm$ in both x and y directions. The measured field distribution validates the simulated ones. It should also be noted that the field concentration near the base of the cone is not very sensitive to the exact location. In fact, the electric fields remain concentrated within a few centimeters away from the base of the cone. This dual-polarized signal collector is used to build a radiometer system for detection of electromagnetic signaling within biological systems.

## III. Wideband Radiometer System

The receiver attached to the signal collector is similar to that of a very broadband Dicke radiometer whose setup is shown in Fig. 7. The signal from each terminal of the collector is amplified by a broadband low-noise amplifier (RLNA00M50GA from RF-LAMBDA) and is recorded by a spectrum analyzer. Since the measurement can take up to several days, the gain of the amplifier may change over time. In order to eliminate the gain fluctuations of the amplifier, a SPDT switch (Mini-Circuits MSP2T-18XL+) is placed between the signal collector and the input of the amplifier. The other port of the switch is terminated with a 50 Ω matched load which serves as a constant (reference) noise source. The switch alternates between the signal collector and the matched load and the power measured from both cases are recorded. If the sweep time of the spectrum analyzer is short enough (in the order of millisecond), the gain of the amplifier is assumed constant during two consecutive sweeps. The gain variations of the amplifier can be eliminated by normalizing the power measured from the signal collector to that from the matched load.

The total noise power delivered to the receiver is

$$P_{sys} = k(T_A + T_{rec})BG \tag{5}$$

where $k$ is Boltzmann's constant, $T_A$ is the equivalent noise temperature of the signal collector, $T_{rec}$ is the noise temperature of the receiver alone (excluding the signal collector) referred to the input of the collector, $B$ is the bandwidth and $G$ is the total gain of the receiver. The noise temperature of the receiver is related to its noise factor by

$$T_{rec} = (F_{rec} - 1)T_0 \tag{6}$$

in which $T_0$ is the ambient temperature. The overall noise performance of the receiver is significantly affected by its first stage (i.e., the low noise amplifier (LNA) in our case). Fig. 8 shows the noise figure of the system with one and two LNAs in each receiving patch. With two amplifiers, the noise figure is only 2.5 dB at 10 GHz and remains below 7 dB from 1 to 40 GHz.

The measurement uncertainty (minimum detectable signal) of a superheterodyne receiver of bandwidth $B$ and integration time constant $\tau$ is [16]

$$\Delta T = \frac{T_A + T_{rec}}{\sqrt{B\tau}} \tag{7}$$

In our case where a spectrum analyzer is used as the receiver, the bandwidth $B$ is the resolution bandwidth (RBW), and the integration time is the reciprocal of the video bandwidth (VBW). Hence (7) can be rewritten as

$$\Delta T = \frac{T_A + T_{rec}}{\sqrt{\frac{RBW}{VBW}}} \tag{8}$$

For the system with $\mathrm{RBW} = 1\,\mathrm{MHz}$ and $\mathrm{VBW} = 300\,\mathrm{Hz}$, the sensitivity is plotted in Fig.9. The minimum detectable signal using one and two LNAs are $-184\,\mathrm{dBm/Hz}$ and $-180\,\mathrm{dBm/Hz}$ at 40 GHz respectively, which corresponds to the worst-case scenario. It should be noted that the system sensitivity can be improved by using amplifiers with lower noise figure and/or higher gain, reducing the video bandwidth, and increasing the resolution bandwidth. Furthermore, averaging $N$ traces can reduce the uncertainty by a factor of $\sqrt{N_{trace}}$.

The expression for the uncertainty $\Delta T$ given by (8) does not consider the gain variations of the amplifiers. As described previously, the absolute power measured from the signal collector will be normalized to a reference noise source. Since these two measurements are independent, the uncertainty of the normalized value can be approximated as [17]

$$\Delta R = \sqrt{\left(\frac{T_A + T_{rec}}{T_{ref} + T'_{rec}}\right)^2 \left[\left(\frac{\Delta T}{T_A + T_{rec}}\right)^2 + \left(\frac{\Delta T'}{T_{ref} + T'_{rec}}\right)^2\right]} \tag{9}$$

This article has been accepted for publication in a future issue of this journal, but has not been fully edited. Content may change prior to final publication. Citation information: DOI 10.1109/TIM.2020.2994433, IEEE Transactions on Instrumentation and Measurement


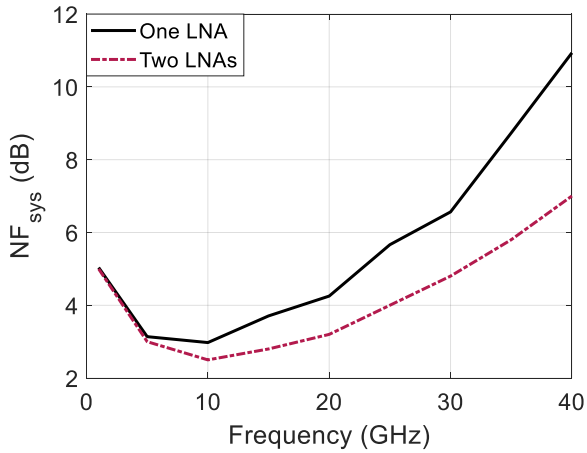


Fig. 8: The measured noise figure of the system.

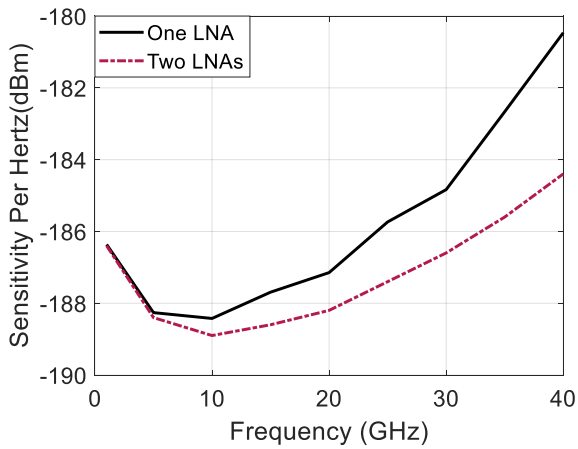


Fig. 9: The sensitivity of the spectrum analyzer-based radiometer when the RBW is 1 MHz and the VBW is 330 Hz.

where $T'_{rec}$ and $\Delta T'$ are respectively the noise temperature of the receiver and the measurement uncertainty when the switch is connected to the matched load. If $T_A = T_{ref} = T_0$ and $T_{rec} = T'_{rec}$, (9) can be simplified to

$$\Delta R = \sqrt{2}\frac{\Delta T}{F_{rec}T_0} = \sqrt{\frac{2VBW}{RBW}} \tag{10}$$

## IV. Measurement of Thermal Radiation from Water

By now, although there are many hypotheses about purposeful electromagnetic wave signaling between biological cells in the literature [1]-[3], no experiments have proved the existence of such signals in the GHz frequency range. The goal of the presented system is to provide a tool to perform the necessary measurements and to explore the existence of electromagnetic emission from biological samples in GHz spectrum. To demonstrate the high sensitivity of the system, it is important to validate its performance using a known radiative source. We measured thermal radiation from 30 milliliter distilled water having different temperatures and estimated the sensitivity of our system. Fig. 10 shows the measurement setup.

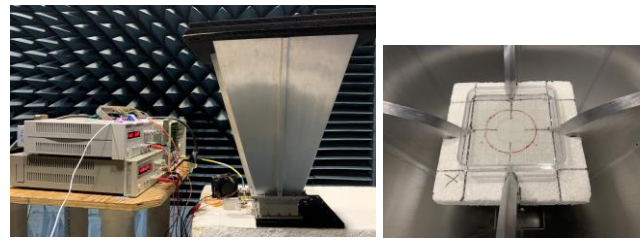

(a) (b)

Fig. 10 (a) The measurement setup and (b) the water sample

The water is contained in the same petri dish (Fisherbrand, $100mm \times 100mm$, Sterile, Polystyrene) used for growing biological samples. Amplifiers with better noise figure (LNF-LNR6 1223Z 6-20 GHz from LOW NOISE FACTORY) are used in this measurement. The resolution bandwidth and video bandwidth of the spectrum analyzer are 2 MHz and 100 Hz, respectively. We first measured the water at room temperature (22℃) as the baseline and gradually increase the temperature of the water until our system can distinguish its thermal radiation from the baseline. The minimum detectable power can be estimated from the temperature difference between the two water samples. The thermal emission measurement exactly mimics the biological sample measurement: the water sample at room temperature is equivalent to the background medium measurement and the increased radiation from the heated water can be considered as the additional emission from the biological samples. Therefore, the minimum detectable power in this setup is the minimum power biological samples should generate for our system to be able to detect.

The brightness temperature of a water layer of thickness $d$ for $p$ (hh or vv) polarization measured at normal incidence is [18]

$$T_{Bw}^{p} = \frac{1-r}{1-r^2e^{-2\kappa_a d}}(1 - re^{-2\kappa_a d})T_w + (1-r)(T_w - T_0)e^{-\kappa_a d} \tag{11}$$

where $T_0$ is the ambient temperature, $T_w$ is the physical temperature of the water, $\kappa_a$ is the absorption coefficient of water, and $r$ is the reflectivity at the boundary between the water and air at normal incidence and is given by

$$r = \left|\frac{\sqrt{\varepsilon_w}-1}{\sqrt{\varepsilon_w}+1}\right|^2 \tag{12}$$

in which $\varepsilon_w$ is the relative dielectric constant of water.

The minimum detectable power per hertz for one polarization is approximately

$$P_{min} = k\left(T_{Bw1}^{p} - T_{Bw0}^{p}\right) = k\Delta T_{Bw}^{p} \tag{13}$$

The minimum detectable physical temperature difference $\Delta T_{Bw}^{h}$ for hh polarization is 13 ℃ above the baseline for a 3 $mm$ water layer from 5-20 GHz. The calculated minimum detectable power as a function of frequency is plotted in Fig. 12. It is shown that the system can detect the change in background emission with a signal level as low as -191 dBm/Hz. The measurement is repeated 10 times and the results at 5, 10 and 15 GHz are shown in Fig. 11(b). Our system can consistently distinguish the thermal radiation from these two water samples even from a single measurement. If average is performed

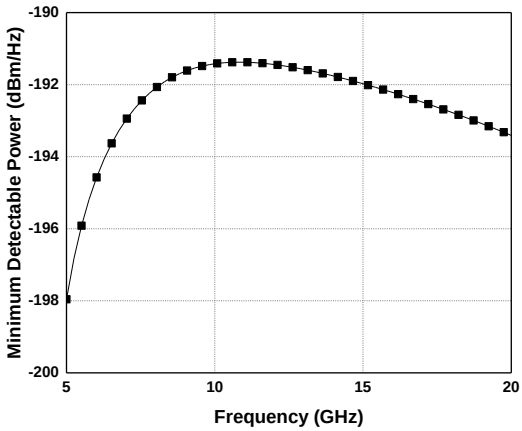


Fig. 11 Calculated minimum detectable power as a function of frequency

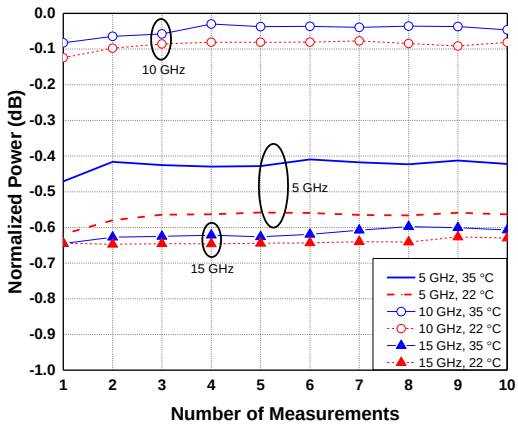


(b)

Fig. 12 Measured normalized power of water samples at 5, 10 and 15 GHz

among all the measurements, the sensitivity of the system can be further improved as explained in Section III.

This exemplary measurement proves that the system is capable of detecting extremely weak electromagnetic radiation and is suitable for the intended applications such as examining the existence of electromagnetic emission from biological samples.

## V. Conclusion

A wideband near-zone radiative system with 1:50 bandwidth ratio and high sensitivity is designed and fabricated to investigate the possible existence of low-power electromagnetic emission from biological samples or other electromagnetic sources from 1 GHz to 50 GHz. The system is composed of a carefully-designed signal collector which can focus the field over an area where the Petri dish containing biological samples is placed, a Dicke switch, a matched load at constant temperature, high-gain low-noise amplifies, and a sensitive wideband spectrum analyzer. It is shown that the system can detect the change in background emission with a signal level as low as -191 dBm/Hz. The system proves to be capable of measuring extremely weak signals, therefore it provides a possibility to perform the necessary measurements of biological samples. Our team is currently conducting experiments on different biological samples and the results will be reported in the future.

## Acknowledgement

This project was supported by DARPA RadioBio program under contract HR00111720067. The NeoScan system used in the measurement was acquired from EMAG Technologies in which Professor Sarabandi is a principal.

## References

[1] D. Havelka, M. Cifra, D. Havelka, and M. Cifra, “Calculation of the Electromagnetic Field Around a Microtubule,” *Acta Polytech.*, vol. 49, no. 2, 2009.

[2] J. Pokorný, J. Pokorný, and J. Kobilková, “Postulates on electromagnetic activity in biological systems and cancer,” *Integr. Biol. (United Kingdom)*, vol. 5, no. 12, pp. 1439–1446, 2013.

[3] A. Widom, J. Swain, Y. N. Srivastava, and S. Sivasubramanian, “Electromagnetic Signals from Bacterial DNA,” no. 2, pp. 1–4, 2011.

[4] V. Ranieri, A. Deutsch, G. V. Kopcsay and G. Arjavalingam, "A novel 24-GHz bandwidth coaxial probe,"*IEEE Transactions on Instrumentation and Measurement*, vol. 39, no. 3, pp. 504-507, June 1990.

[5] M. L. Crawford, "Generation of Standard EM Fields Using TEM Transmission Cells," *IEEE Transactions on Electromagnetic Compatibility*, vol. EMC-16, no. 4, pp. 189-195, Nov. 1974.

[6] D. Pouhe, "RF radiation properties of printed-circuits boards in a GTEM cell," *IEEE Transactions on Electromagnetic Compatibility*, vol. 48, no. 3, pp. 468-475, Aug. 2006.

[7] S. Deng, T. H. Hubing and D. G. Beetner, "Using TEM Cell Measurements to Estimate the Maximum Radiation from PCBs With Cables Due to Magnetic Field Coupling," *IEEE Transactions on Electromagnetic Compatibility*, vol. 50, no. 2, pp. 419-423, May 2008.

[8] T. Loh and M. J. Alexander, "A Method to Minimize Emission Measurement Uncertainty of Electrically Large EUTs in GTEM Cells and FARs Above 1 GHz," *IEEE Transactions on Electromagnetic Compatibility*, vol. 48, no. 4, pp. 634-640, Nov. 2006.

[9] Zhen Ji, C. Hagness, H. Booske, S. Mathur and M. L. Meltz, "FDTD analysis of a gigahertz TEM cell for ultra-wideband pulse exposure studies of biological specimens," *IEEE Transactions on Biomedical Engineering*, vol. 53, no. 5, pp. 780-789, May 2006.

[10] P. Alotto, D. Desideri, F. Freschi, A. Maschio and M. Repetto, "Dual-PEEC Modeling of a Two-Port TEM Cell for VHF Applications," *IEEE Transactions on Magnetics*, vol. 47, no. 5, pp. 1486-1489, May 2011.

[11] S. Deng, D. Pommerenke, T. Hubing and D. Shin, "An Experimental Investigation of Higher Order Mode Suppression in TEM Cells," *IEEE Transactions on Electromagnetic Compatibility*, vol. 50, no. 2, pp. 416-419, May 2008.

[12] DARPA. (2017, Feb. 2). RadioBio: What role does electromagnetic signaling have in biological systems? [Online]. Available: https://www.darpa.mil/news-events/2017-02-07.

[13] W. Sun and C. A. Balanis, "Analysis and design of quadruple-ridged waveguides," *IEEE Transactions on Microwave Theory and Techniques*, vol. 42, no. 12, pp. 2201-2207, Dec. 1994.

[14] J. Kerr, "Short axial length broad-band horns," *IEEE Transactions on Antennas and Propagation*, vol. 21, no. 5, pp. 710-714, September 1973.

[15] https://emagtech.com/neoscan-system/.

[16] F. Ulaby and D. Long, *Microwave Radar and Radiometric Remote Sensing*, Ann Arbor, (Michigan): The University of Michigan Press, 2014, ch. 7, pp. 263-323.

[17] “Approximations for Mean and Variance of a Ratio.” https://www.stat.cmu.edu/~hseltman/files/ratio.pdf

[18] Leung Tsang Jin Au Kong Kung-Hau Ding, “Scattering and Emission by Layered Media,” in *Scattering of Electromagnetic Waves: Theories and Applications*, John Wiley & Sons, Ltd, 2000, pp. 199–229.